



Article

The Potential of the Horizontal Component TEM Data in the Detection of Polarizable Mineral: Synthetic Cases

Yanqi Wu ^{1,*} , Huilin Xie ¹, Yanju Ji ², Peng Zhao ^{1,*}  and Yuebing Wang ¹¹ College of Metrology and Measurement Engineering, China Jiliang University, Hangzhou 310018, China² College of Instrumentation and Electrical Engineering, Jilin University, Changchun 130026, China

* Correspondence: wuyanqi@cjlu.edu.cn (Y.W.); zhaopeng@cjlu.edu.cn (P.Z.)

Abstract: Induced polarization (IP) effects in transient electromagnetic (TEM) measurement play a significant role in the detection of minerals, such as sulfide ore, clay ore, etc. However, due to the complex impacts caused by the polarization parameters, the structure of the earth, and the measurement system configuration, the IP effects cannot be easily measured and interpreted. We paid more attention to the vertical component of the ungrounded-TEM system in previous work; however, we will now attempt to utilize the horizontal component to enhance the precision of the measurement and interpretation. We quantitatively discussed the behavior of the horizontal and vertical magnetic fields of the towed-TEM (tTEM) system. We simultaneously introduced the vertical and horizontal components into the Jacobian matrix of the 1D laterally constrained inversion to build the joint inversion. Compared to the vertical component, the horizontal component always shows earlier and bigger sign reversals and contains more IP information. Inversion with the single horizontal or single vertical component showed poor accuracy in the deep and shallow layers, respectively. The joint inversion with both components could correct the errors. Including the horizontal component in the detection and interpretation facilitates an improved resolution for polarizable minerals.

Keywords: polarizable minerals; the towed-TEM system; the joint inversion; the horizontal component



Citation: Wu, Y.; Xie, H.; Ji, Y.; Zhao, P.; Wang, Y. The Potential of the Horizontal Component TEM Data in the Detection of Polarizable Mineral: Synthetic Cases. *Minerals* **2023**, *13*, 523. <https://doi.org/10.3390/min13040523>

Academic Editor: Stanislaw Mazur

Received: 26 December 2022

Revised: 22 March 2023

Accepted: 5 April 2023

Published: 7 April 2023



Copyright: © 2023 by the authors. Licensee MDPI, Basel, Switzerland. This article is an open access article distributed under the terms and conditions of the Creative Commons Attribution (CC BY) license (<https://creativecommons.org/licenses/by/4.0/>).

1. Introduction

The transient electromagnetic (TEM) method has been applied in mineral resource exploration and environmental monitoring [1–4]. The induced polarization (IP) effect, a significant electrochemical phenomenon, can exist in porous media, such as massive sulfide disseminated ores, water, electrolyte, and even in the frozen-soil zone [5,6]. The IP effect is associated with the storage of electrical charges caused by the electromigration of charge carriers (electrons and ions) in porous materials. At the present stage, much research has shown evidence of the IP effects that appear in what is called the negative response phenomenon within the TEM responses [7,8]. Recently, interest in recovering IP parameters from the TEM (TEM-IP) data has increased considerably, which has also lead to a breakthrough in some significant applications, such as the exploration of minerals, hydrocarbons, water resources, etc. [9–14]. Moreover, high-precision detection and interpretation has extended the application of the TEM-IP method to the monitoring of permafrost, groundwater pollution, and weathered geology [15–17].

Concomitant with the IP effects in porous media, the electrical conductivity is frequency dependent. So far, no universal physical–chemical model has been developed to describe the frequency dispersion; researchers proposed many models obtained by fitting spectra curves at low frequencies, such as the Dias model [18], the Debye model [19], the Cole–Cole model [20], etc. Along with the deep-going research, a more accurate model known as the generalized effective medium theory for induced polarization (GEMTIP) model is proposed [21]. Many surveys confirmed that the negative response or sign reversal observed can be verified by simulation based on the Cole–Cole model [22–24]. Therefore, we also use it to examine TEM-IP parameters that are related to physical properties:

$$\rho(\omega) = \rho_0 \left[1 - m_0 \left(1 - \frac{1}{1 + (i\omega\tau_\rho)^c} \right) \right] \quad (1)$$

where ω describes the angular frequency, ρ_0 describes the DC resistivity of the earth, and m_0 is the chargeability, which describes the degree of charge accumulation of the earth. τ_ρ is the relaxation time, which describes the time required for charge accumulation to reach equilibrium; c is the frequency exponent, which describes the broadness of the relaxation time distribution; τ_ρ and c define the rate of charge accumulation, but the impact of c is smaller compared with τ_ρ . Determined by these parameters, the IP effect manifests sign reversals in the TEM data. Many researchers have theoretically studied the vertical component under the ungrounded-TEM system and found m_0 , τ_ρ , and c greatly affect the occurrence time of sign reversal (Time of SR) and the maximum amplitude of negative responses (max of NR) [25]. In theory, when m_0 is larger, τ_ρ is smaller and c is around 0.5, which means the medium has a strong ability to accumulate electric charges and a faster rate of charge accumulation; therefore, the Time of SR occurs earlier and the amplitudes of NR are larger [26]. Several locations where IP effects are reported and recorded demonstrated that the range of each parameter varies hugely. Some minerals present strong IP effects, such as disseminated sulfide, clay layers, and shallow frozen rocks [27], that are likely to present the IP features apparently. Conversely, some mediums with relatively weak IP effects (m_0 is below 0.1) usually cause the EM data not to show the IP features [28]. Once the IP information is missing, it will be tough to recover the parameters accurately, especially for the weak IP effects [29].

For chargeable target imaging, the measurement and extraction of IP information contained in TEM data has been studied in detail. To extract the IP information, Chen et al. developed a robust way to extract the subtle polarization responses [30], Fiandaca et al. performed re-parameterizations of the Cole–Cole model before inversion to increase the resolution [31], and Kang and Oldenburg proposed a method for extracting more IP information by decoupling the EM and IP responses [23]. Some surveys tried to enhance the IP information from the instrument aspect, such as different TEM systems, transmitter frequencies, the time derivative of the magnetic field versus the magnetic field, and the turn-off time [32,33]. Kirkegaard et al. found that adding a helicopter system x-component to a 1D inversion can facilitate higher confidence in the layered resistivity-inversion [34]; Wang et al. studied the characteristic curve of the horizontal component and found it can effectively point to the central direction of the low-resistivity ore body [35]. Their study only focused on the accuracy of resistivity inversion and did not evaluate the inversion of polarization media. Jang et al. used the in-loop system to analyze the horizontal and vertical fields of the IP responses and claimed that the target signal is larger and appears early in the horizontal magnetic fields than in the vertical magnetic fields; however, the inversion resolution of using the vertical magnetic component is higher than that of using the horizontal field [36]. The potential of the horizontal component in the detection of IP effects has not been fully explored.

In the synthetic study, we proposed a joint-component inversion method to improve the inversion resolution of polarization parameters. Unlike the previous work, in which only the vertical component was recovered, we added the horizontal component to the 1D laterally constrained inversion (LCI) scheme to invert the polarization parameters. Moreover, we discussed the range of chargeability that can be recovered.

2. Methods

2.1. The tTEM System and Noise Level

We performed the forward and inversion process based on the towed TEM (tTEM) system configuration [37]. The tTEM system used in the simulations was capable of imaging the subsurface down to a depth of 70 m with a high horizontal and vertical resolution. As shown in Figure 1, towed by an all-terrain vehicle (ATV), the system used a 2×4 m transmitter coil horizontally. Two coils were used as one horizontal component and one

vertical component receiver, respectively, which were offset 9 m from the transmitter in the x-direction. The transmitter current was 30 A and the first bias-free gate was as early as 4 μs from the beginning of the ramp (1.4 μs after the end of the ramp). The tTEM system was able to measure multi-components simultaneously, which shows the experiment’s advantages in conducting joint inversion.

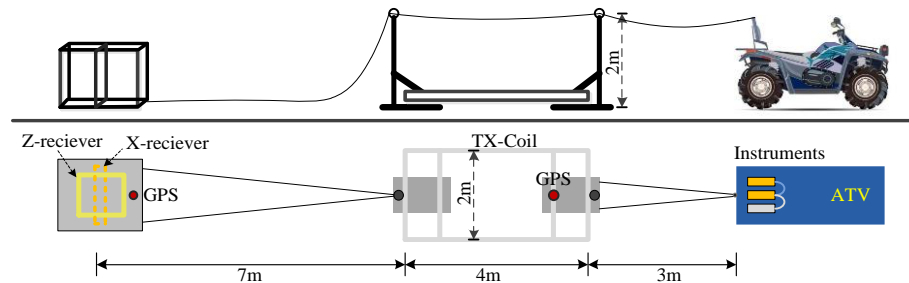


Figure 1. The schematic of the tTEM system.

The noise model in synthetic modeling was the same as that of Auken et al. [38], which is described in the equation,

$$V = G(0,1) \cdot \left[\text{STD}_{\text{uni}}^2 + V_{\text{noise}}^2 \right]^{\frac{1}{2}} \tag{2}$$

where $G(0,1)$ is the Gaussian distribution with zero mean and standard deviation 1, $\text{STD}_{\text{uni}}^2$ represents the uniform noise, and V_{noise} represents the background noise contribution. STD, the uniform standard, is set to 3% for dB/dt responses typically, which accounts for the instrument and other non-specified noise contributions. The background noise that decreases with $t^{-1/2}$ in transients is given by,

$$V_{\text{noise}} = b \cdot \left(\frac{t}{10^{-3}} \right)^{-\frac{1}{2}} \tag{3}$$

where b is the noise level at 1 ms.

Under the horizontal transmitter loop, the vertical component of the magnetic field was less disturbed by the background noise; however, the horizontal component of the magnetic field was heavily disturbed by the background noise. According to the literature, the noise level of the x -component would be 5–10 times larger than the z -component [34,39,40]. Based to the tTEM system parameters, we set $b = 0.2 \text{ nV/m}^2$ and $b = 1.6 \text{ nV/m}^2$ at 1 ms for z and x components, respectively.

2.2. Forward Modeling Process

We used the AarhusInv code to simulate the EM data [41]. The EM data was induced by a horizontal electric dipole at the earth’s surface; using either a whole uniform space or a layered model, it was calculated by the expression presented by Ward and Hohmann [42]. We first calculated the responses in the frequency-domain, before obtaining the time-domain results by the fast inverse Fourier transformation.

The model space of the Cole–Cole parameters is defined as follows:

$$m_{\text{resistivity-Cole-Cole}} = \{ \rho_0, m_0, \tau_\rho, c \} \tag{4}$$

Following the study of Fiandaca et al., we also used the maximum phase angle (MPA) model to eliminate correlation between the Cole–Cole parameters [31]. The model space of MPA parameters is defined as follows:

$$m_{\text{MPA}} = \{ \rho_0, \varphi_{\text{max}}, \tau_\varphi, c \} \tag{5}$$

where φ_{max} represents the maximum phase angle of the Cole–Cole model and τ_φ is the

inverse of the frequency at which φ_{\max} is reached. The relaxation time τ_φ is linked to τ_ρ through m_0 and c , as follows: $\tau_\varphi = \tau_\rho(1 - m_0)^{1/2c}$.

We calculated the time derivatives of the vertical magnetic (dB_z/dt) and horizontal fields (dB_x/dt) of 1D layered models with or without the IP effects. To analyze the behavior of different EM components, we compared the negative value and slope of TEM responses and quantified the influence of the IP effects on the EM data by calculating the direct impact ratio [29]:

$$\zeta(t) = \frac{M_{IP}(t)}{M_{non-IP}(t)} \tag{6}$$

where $\zeta(t)$ represents the direct impact ratio, M_{IP} represents the EM data with the IP effects (IP responses), and M_{non-IP} represents the EM data without the IP effects (non-IP responses). If the ratio is around 1, the difference between IP responses and non-IP responses is little and, thus, the response is barely affected by the IP effects. If sign reversal appears, the value will drop to negative values. Figure 2 shows an example of the IP responses of a three-layer chargeable model.

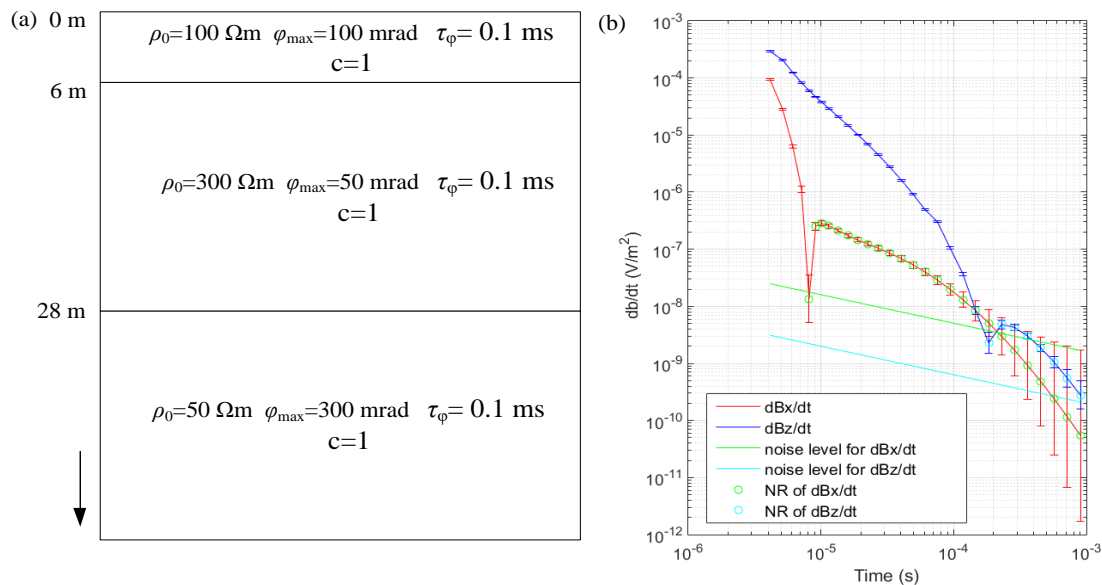


Figure 2. IP responses for a three-layer model. (a) The three-layer model. (b) The time derivatives of the magnetic fields, where red curves represent dB_x/dt with the errorbar, blue curves represent dB_z/dt with the errorbar; and the negative values are marked with green circles or cyan circles, respectively. Moreover, the green and cyan lines show the noise levels: b takes 1.6 and 0.2 nV/m^2 at 1 ms for x and z components, respectively. The errorbars are connected with the noise model described in Equation (2).

2.3. 1D Laterally Constrained Inversion Scheme

In this study, we used a 1D LCI scheme to invert the 1D forward responses and tie the models together into a pseudo-2D layered model. Due to the lateral constraints, information from one model diffused to neighboring models. The lateral constraints were considered as priori information on the geological variability. The main expected outcome of the 1D-LCI was not only the creation of pseudo-2D images, but also an enhanced model resolution in the deepest parts of the model corresponding to late decay times [43].

The model space was set up with the logarithms of the MPA parameters and the thicknesses for all the layers of each model:

$$\mathbf{m} = \left[\begin{array}{l} \{ \log(\rho_{i,j}), \log(\varphi_{\max i,j}), \log(\tau_{\varphi i,j}), \log(c_{i,j}), \log(thk_{i,k}) \}, \\ i = 1, \dots, N_{\text{models}}; j = 1, \dots, N_{\text{layers}}; k = 1, \dots, N_{\text{layers}} - 1 \end{array} \right] \tag{7}$$

The 1D-LCI approach minimized a common objective function that included lateral constraints between adjacent models as well as constraints to the start values of the model, the depths of layers, and vertical and horizontal constraints.

The inversion was performed iteratively following the established practice of linearized approximation with the first term of the Taylor expansion.

$$d_{\text{obs}} + e_{\text{obs}} \cong G(m_{\text{ture}} - m_{\text{ref}}) + g(m_{\text{ref}}) \tag{8}$$

where d_{obs} denotes the observed data, e_{obs} denotes the error on the observed data and g is the forward mapping. The Jacobian matrix G contains the partial derivative of the forward mapping with respect to the model parameters. The previous method introduced a single vertical component to the Jacobian matrix G ; however, we have made a little improvement on the basis of previous work by introducing both vertical and horizontal components into G for the joint inversion. Equation (8) also can be written as

$$G\delta m_{\text{ture}} = \delta d_{\text{obs}} + e_{\text{obs}} \tag{9}$$

where δd_{obs} represents the differences between observed data and forward data. The covariance matrix for the observation errors C_{obs} can be calculated by d_{obs} and $g(m_{\text{ref}})$.

The constraints were connected to the true model as

$$R\delta m_{\text{ture}} = \delta r + e_r \tag{10}$$

where e_r is the errors on the constraints between adjacent points with 0 as the expected value; $\delta r = -Rm_{\text{ref}}$ provides the identity between the parameters tied by constraints in the roughening matrix R , containing 1 and -1 for the constrained parameters, 0 in all other places. The variance, or strength of the constraints, is described in the covariance matrix C_R . Practical experiments showed that constraint values between 1.1 and 1.3 were good starting options. Roughly speaking, a constraint value of 1.1 meant those model parameters were allowed to vary by 10% between neighboring models. Thus, if we combine Equations (9) and (10), we can find

$$\begin{bmatrix} G \\ R \end{bmatrix} \delta m_{\text{ture}} = \begin{bmatrix} \delta d_{\text{obs}} \\ \delta r \end{bmatrix} + \begin{bmatrix} e_{\text{obs}} \\ e_r \end{bmatrix} \tag{11}$$

Thus the inverse problem is written as

$$G'\delta m_{\text{ture}} = \delta d' + e' \tag{12}$$

And the covariance matrix of the inversion C' that contains C_{obs} and C_R is written as:

$$C' = \begin{bmatrix} C_{\text{obs}} & 0 \\ 0 & C_R \end{bmatrix} \tag{13}$$

The update model and objective function minimized in the inversion process are expressed by Equations (14) and (15), respectively:

$$m_{(n+1)} = m_{(n)} + [G'_{(n)}{}^T C'^{-1} G'_{(n)}]^{-1} \cdot G'_{(n)}{}^T C'^{-1} \delta d' \tag{14}$$

$$Q^* = \left(\frac{\delta d'^T C'^{-1} \delta d'}{N_d + N_m + N_r} \right)^{1/2} \tag{15}$$

where $\delta d'$ contains δd_{obs} and δr , while N_d , N_m , and N_r represent the number of data points, model parameters, and constraints. The data misfit χ can be calculated by

$$\chi = \left(\frac{\delta d_{\text{obs}}^T C_{\text{obs}}^{-1} \delta d_{\text{obs}}}{N_d} \right)^{1/2} \tag{16}$$

In the inversion process, a homogeneous starting model was used, while the stopping criterion for the inversion was a relative change in the objective function below 1%. A detailed description of the inversion algorithm and the practical implementation of the constraints was given by Auken and Christiansen [43]. In the inversion, we can specify to perform either the x or z , or x and z components inversion process, and choose to perform resistivity or MPA inversion; for example, when choosing the MPA inversion with the x and z components, the code simultaneously inverted dB_z/dt and dB_x/dt , calculated $\delta \mathbf{d}'$ covariance matrix C' to obtain Q^* , and updated the estimated model finally.

The appearance time of sign reversal in the late time inferred large variation in the data misfit and leads to instability, which could easily trap the model in a local minimum. To mitigate the effects, we increased the uniform STD on the four-time gates around the sign reversal(s) from 3% to 30%. The total STD was the sum of the STD on the noise model and the STD on the negative value modified by the scaling factor. If the measured data was heavily disturbed by noise, it should have been excluded from further analysis and inversion, whether the value is negative or positive [44]. In practice, the data were removed when the total STD of the data was larger than 30% because the data could not be used. The remaining data were then delivered to the inversion process.

2.4. The Synthetic Models and Sounding Layout

To compare the differences between the behaviors of the x versus z components and investigate the impact ratios of the IP effects, we simulated the EM responses with the IP effects of different intensities. In total, 16 synthetic models were combined into a pseudo-2D layered model, as shown in Figure 3. The middle layer was located 6 m below the surface and its shape looked like a jagged triangle; the thickest depth was at 32 m. We also noted that the model was fairly 1D with a small 2 m drop on the second layer between neighbors. The third layer was located diagonally at the left of the second layer. Here, the distance between the adjacent model was 10 m. We chose the parameters for each synthetic model according to actual field conditions. The ranges of strong and moderate polarization parameters came from frozen sediment, clay sediment, and sulfide ore according to two past studies [15,16], while the ranges of subtle polarization parameters came from TDIP inversion results of the Eskelund landfill, Denmark [45]. The parameters of the strong, moderate, and subtle chargeable mediums are shown in Table 1. The first synthetic model involved the near-surface frozen sediment and revealed high-resistivity and high-polarization properties, while the second synthetic model was related to clay sediment or sulfide ore (low-resistivity, high-polarization medium), which was embedded in a high-resistivity, low-polarization surrounding rock; the third synthetic model was related to landfill field where the second layer was more conductive and polarizable due to infiltration of domestic waste. Setting $c = 0.5$ for the three cases, overall, m_0 was the largest and τ was the smallest for the strong chargeable medium, while m_0 was the smallest and τ was the largest for the subtle chargeable medium. The parameters in the moderate chargeable medium were at the middle level.

Table 1. The parameters of the synthetic three-layered chargeable models.

MPA Parameters	Layer	ρ_0 (Ωm)	φ_{max} (mrad)	τ_φ (ms)	c
Strong chargeable medium	1	100	100	0.1	0.5
	2	300	50	0.1	0.5
	3	50	300	0.1	0.5
Moderate chargeable medium	1	150	80	0.1	0.5
	2	300	50	0.1	0.5
	3	10	100	0.1	0.5
Subtle chargeable medium	1	100	10	100	0.5
	2	30	30	100	0.5
	3	100	10	100	0.5

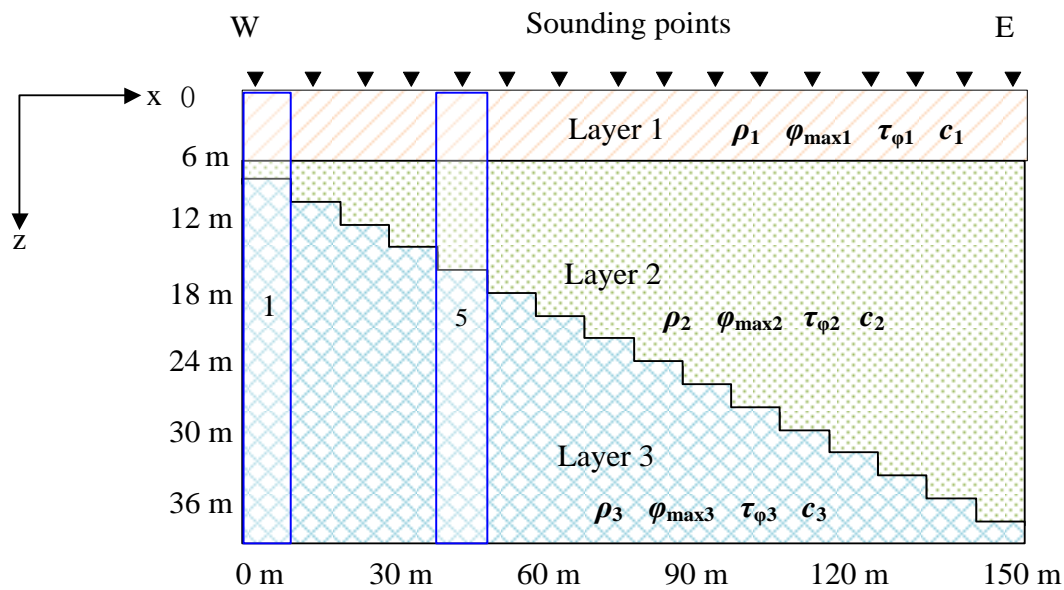


Figure 3. Synthetic models and sounding points. For example, the blue boxes present model 1 and model 5.

3. Results and Discussion

In this section, we focus on the sensitivity and inversion ability of the x component in revealing the IP effects. The results show the forward responses and inversion results of the strong chargeable medium, moderate chargeable medium, and subtle chargeable medium. We investigate the potential of the horizontal component in detecting the IP effects from three aspects: (1) comparison between the polarization features of x -component EM responses with those of z -component EM responses; (2) quantification of the impact degree of the IP effects; (3) evaluation of the inversion ability of single components and joint components.

3.1. Comparison of between Horizontal and Vertical Components of Forward Modeling

3.1.1. Synthetic Model 1: Strong Chargeable Medium

Figure 4 presents the x - and z -component EM responses and the direct impact ratio ζ . In Figure 4a, the x -component shows that the amplitude is one-fifth of the z -component, while the noise level is eight times higher than that of the z -component. However, the x -component decays with at least twice the decay rate of the z -component. The signal noise ratio (SNR) of the x -component is 32 dB lower than that of the z -component within the same tTEM system, which brings a greater limit in the application of the x -component and means that we must consider the influences of the noise level. Moreover, the IP data is seriously affected by the noise because the broad dynamic range of the signal may exceed that of the receiver. We definitely found that both z - and x -components apparently reveal steep decays and sign changes before falling into noises; this is especially true for the x -component. More specifically, the negative responses of the x -component first appear at 7 μ s, whereas negative responses of the z -component appear after 100 μ s; the maximum absolute value of negative responses of the x -data is 1.8 μ V/m² (SNR = 40 dB), whereas that of the z -data is 0.025 μ V/m² (SNR = 34 dB). The horizontal component shows the IP features more clearly.

In practice, the data will be removed when the total STD is larger than 30% because the data cannot be used. After removing the noisy data, the z -data left about 25 gates (the last time is 0.36 ms), whereas the x -data left about 20 gates (the last time is 0.12 ms). Furthermore, we plotted the direct impact ratio ζ with the same color bar in Figure 4c,d. ζ is an important parameter to weigh the degree of electromagnetic field affected by the IP effects. At early time, ζ is larger than one, which means the M_{IP} is larger than M_{non-IP} ; over time, ζ decreases to one, which means $M_{IP} \approx M_{non-IP}$. ζ then decreases to zero or even

negative values, which means M_{IP} is a negative value. The x component shows a wide range of ζ varying from 3 to -10 and the z component ranges from 3 to -3 . The degree of polarization influence is proportional to the difference between ζ and 1. Hence, compared with the conventionally measured vertical component, the horizontal component is more susceptible to the IP effects and shows IP features more obviously.

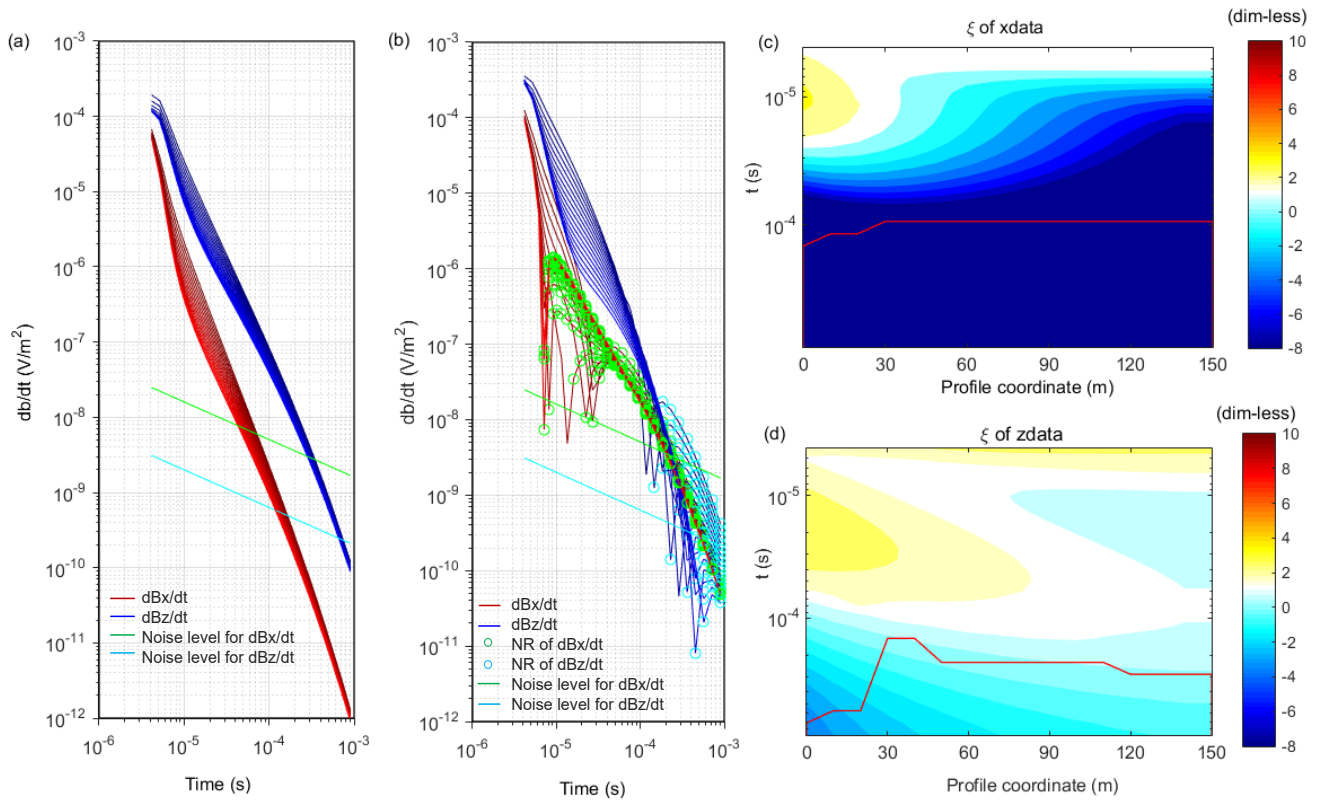


Figure 4. Results of forward modeling for the strong chargeable medium: (a) non-IP responses and (b) IP responses, where red curves represent dB_x/dt , blue curves represent dB_z/dt (the color becomes darker from W to E), and negative values are marked with green circles or cyan circles, respectively. Moreover, the green and cyan lines show the noise levels for x - and z -components, respectively; (c) ζ for the x - component; and (d) ζ for the z -component, where the area under the red curve represents the data below the noise level.

3.1.2. Synthetic Model 2: Moderate Chargeable Medium

The results of the moderate chargeable medium are shown in Figure 5. From Figure 5b, we can see the x -component is affected by the IP effects and shows rapid decay and negative values with $SNR \approx 30$ dB, whereas the z -component barely shows any changes. After removing the noisy data, the valid data of the x -component left 15–20 gates, while 28 gates of the z -component are preserved. Moreover, ζ of the z -component (Figure 5d) changes from 2.8 to 0.8. At the same time, the x -components seem to have a wider range of ζ that ranges from 1.4 to -1.6 . Compared with the strong chargeable medium (Figure 4), the IP features in the moderate chargeable medium dwindle because the negative responses appear later and the range of ζ is narrower. Fortunately, the x -component seems to maintain the sensitivity and advantages in revealing the IP features. An example of the subtle IP effect is presented below.

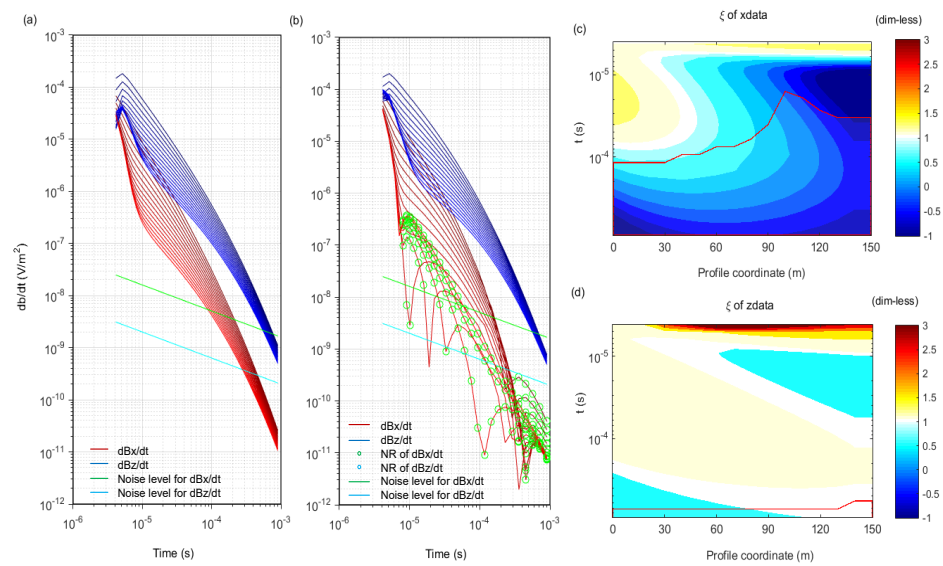


Figure 5. Results of forward modeling for the moderate chargeable medium: (a) non-IP responses and (b) IP responses; (c) ξ for the x -component; and (d) ξ for the z -component. The meanings of the curves and area are the same as in Figure 4.

3.1.3. Synthetic Model 3: Subtle Chargeable Medium

Figure 6 presents the EM data and ξ of the subtle IP medium. As shown in Figure 6, the subtle IP effects have small influences on the EM data, but they do exist. We found that the x -component shows steep decay and negative values which are below the noise level. However, these data have exceeded the measurable range, although the x -component is more sensitive to the IP effects. The IP responses of the z -component seem to be the same as the responses without the IP effects. We investigated the direct impact ratio to quantify the effects of the subtle IP effects. The valid data of the x -component left is 17 gates, whereas that of the z -component is 27 gates. The values of ξ of the x - and z -components vary from 1.32 to 1.18 and 1.23 to 1.08, respectively. The ranges of ξ reduced to around one, which proves that the subtle IP effects have a small impact and the EM responses contain little polarization information. Hence, it seems that the advantages of the x -component in revealing the IP effects diminish.

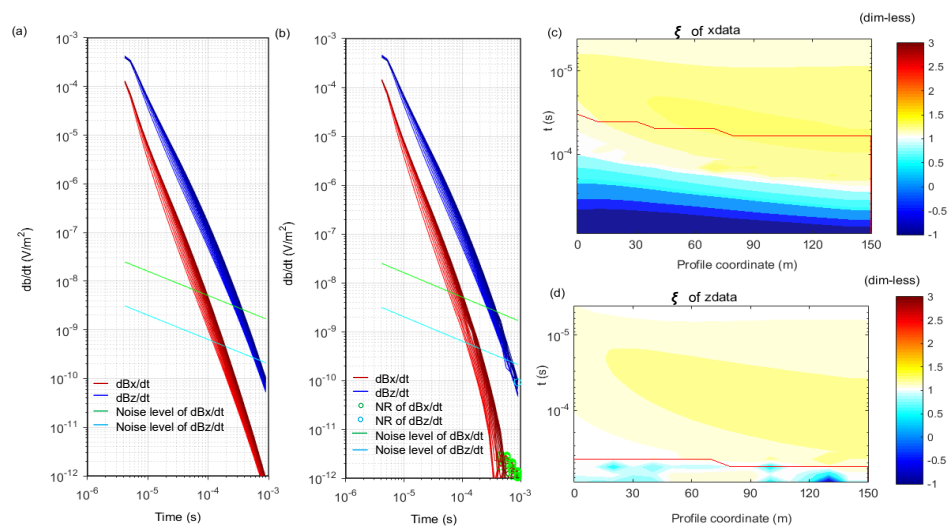


Figure 6. Results of forward modeling for the subtle chargeable medium: (a) non-IP responses and (b) IP responses; (c) ξ of x -component; and (d) ξ of z -component. The meanings of the curves and area are the same as in Figure 4.

3.2. Resolution of *x*-Only, *z*-Only, and Joint Inversion

The *x*-component shows that it is more susceptible to the IP effects; thus, we will utilize the *x*-component to recover the MPA parameters. The inversions with the 1D LCI scheme were conducted by either a single component (*x* or *z*) or both *x*- and *z*-components. To simulate the measured data, we superimposed the uniform and background noise on the forward responses, as shown in Equations (2) and (3). In the data processing program, when the total STD value of the data is greater than 30%, the data will be discarded. We choose the starting MPA Cole–Cole parameters based on the setting guiding method by Lin et al. [18]. That process involves: (1) inverting resistivity-only to include only the non-negative data and using tight lateral and vertical constraints to build a nearly homogeneous resistivity model as the starting value for ρ_0 ; (2) choosing a low or moderate value (10–30 mrad) as the starting φ_{\max} ; (3) setting the starting value for *c* to 0.5, i.e., an intermediate value; (4) selecting a value in the interval 10 μ s to 0.1 s for τ_φ based on the appearance time of sign reversal. For the first two synthetic models, in which ρ_0 varies between 10 Ω m and 300 Ω m and φ_{\max} varies between 50 mrad and 100 mrad, $\tau_\varphi = 0.1$ ms and *c* = 0.5; thus, the starting model is $\rho_0 = 100$ Ω m, $\varphi_{\max} = 30$ mrad, *c* = 0.5, and $\tau_\varphi = 0.1$ ms due to the fact that the sign reversals have arisen early on. For the second model, in which ρ_0 varies between 30 Ω m and 100 Ω m and φ_{\max} varies between 10 mrad and 30 mrad, $\tau_\varphi = 100$ ms and *c* = 0.5 and the starting model is $\rho_0 = 100$ Ω m, $\varphi_{\max} = 10$ mrad, *c* = 0.5, and $\tau_\varphi = 10$ ms because the sign reversal appeared late. However, in some cases the resistivity of the starting model can be hard to retrieve automatically and has to be manually set. We also implemented a robust concept for the calculation of the depth of investigation (DOI) that is valid for any 1D EM geophysical model [46]. The DOI is crucial for interpreting the geophysical models, as the validity of the model varies considerably with data noise and parameter distribution. Therefore, we plotted the inverted results together with DOI information. The DOI visualization was performed by lining the model with a low relative threshold value of 2% (deep).

3.2.1. Synthetic Model 1: Strong Chargeable Medium

We first investigated the impact of ignoring the IP effects in the inversion of polarizable minerals. Figure 7 shows the resistivity-inversion results of the IP responses in the strong chargeable medium. The results show that performing resistivity inversion for the strong chargeable medium cannot effectively match the true model, whether in magnitude or shape, especially in the appearance of high-resistivity artifact (the bottom left corner) in the most conductive layer. The estimated values under the DOI lines are not reliable. Moreover, residuals of the three inversions rise to high magnitudes. Compared to Figure 7c,d, the inversion results of the *x*-data (Figure 7b) demonstrate the worst accuracy with a data misfit value of 13.3; even the deep layers cannot be identified. Figure 7c,d present a rough outline of the model, albeit with low accuracy. We attribute the errors to the portions of the third layer. To determine whether the high-resistivity artifact is caused by the neglect of the IP effects, the inherent multiplicity of solutions, or the instability of the inversion algorithm, we present the resistivity-inversion results of the *x*-component, *z*-component, and *x*- and *z*-component of non-IP responses in Figure 8. The estimated resistivity profiles do not show high-resistivity artifacts. The data misfit in Figure 8 is about 0.3. The resistivity inversion for the non-IP responses can effectively match the true model. We also note that the resolution in the deep layer of *x*-component inversion is not perfect. Hence, even the real resistivity value cannot be obtained if we ignore the IP effect.

Figure 9 shows the results of the MPA-inversion in the strong chargeable medium using a single component and two components. The MPA parameters in Figure 9 are effectively recovered in both magnitude and shape, while the misfits are lower. The estimated value of resistivity is closer to the true value, while the high-resistivity artifact is eliminated to a large extent compared with Figure 7. The profile of φ_{\max} shows that the estimated values in the third layer are smaller than the true values. The residuals of *z*-data and joint inversions are lower than the residuals of *x*-data inversion. From Figure 9b,

we learn that the magnitude of resistivity in the third layer is inaccurate, while the DOIs in ϕ_{max} , τ_{ϕ} , and c are the most shallow (almost 30 m). Comparing Figure 9c,d, we can see that although the residuals are very close (both are around one), the estimated values show differences. The results of ϕ_{max} and ρ_0 in the joint inversion show the three-layered structure more clearly, while in the z -data inversion results the boundary between the first and second layers is blurred. It seems that joint inversion will improve the precision of the shallow layer.

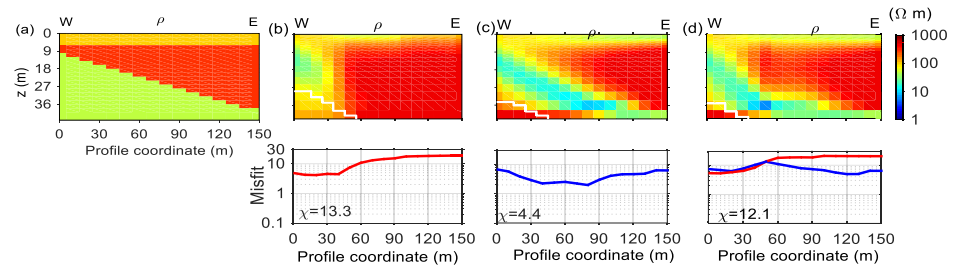


Figure 7. Comparison between the true resistivity value (a) and resistivity inversion results of the IP responses of the strong chargeable medium: by x -data only (b); z -data only (c); and x and z data (d). White line shows the DOI curve and circles the areas of the models below the DOI, while red and blue curves represent the misfits of x data and z data.

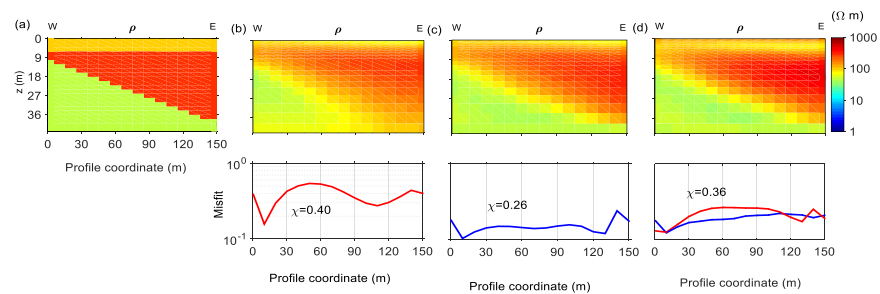


Figure 8. Comparison between the true resistivity value (a) and resistivity inversion results of the non-IP responses of the strong chargeable medium: by x -data only (b); z -data only (c); and x and z data (d). The meanings of the curves and the area are the same as in Figure 7.

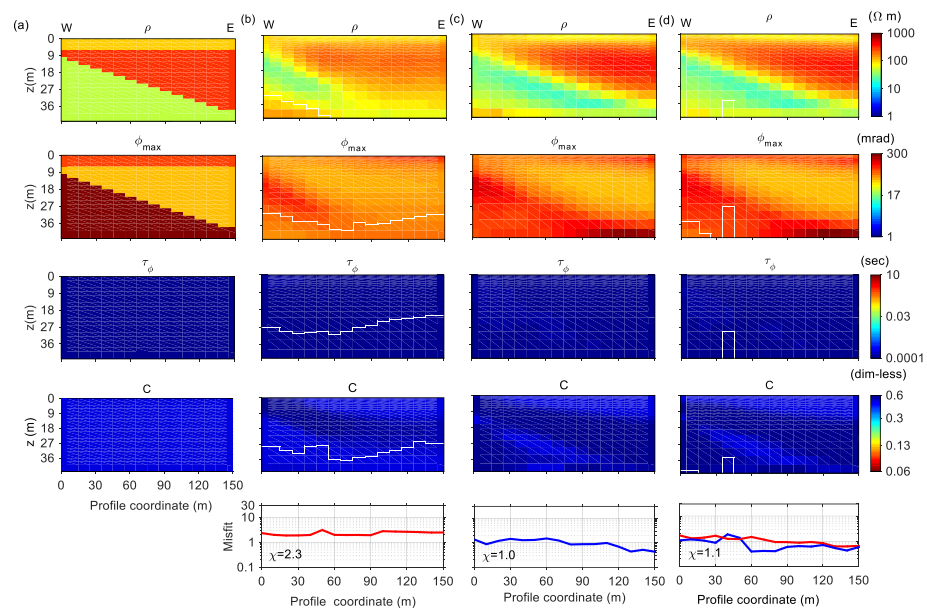


Figure 9. Comparison between the true model (a) and estimated MPA parameters of the strong chargeable medium by x -data only (b); z -data only (c); and x and z data (d). The meanings of the curves and the area are the same as in Figure 7.

3.2.2. Synthetic Model 2: Moderate Chargeable Medium

Figure 10 presents the resistivity-inversion results of the IP responses in the moderate chargeable medium. When using the z -data to conduct the resistivity inversion, the resolution of resistivity is superior compared to the x -data and joint inversion. Apart from the resistivity value of the second layer being larger than the true value, the estimated values between the resistive (the 2nd) and conductive (the 3rd) layers present an abnormal reduction, which means the boundary effect is more serious. Moreover, the residuals increase near the outliers but are lower compared to Figure 7. We also present the results of the resistivity-inversion of the non-IP responses of Model 2 in Figure 11. Compared with Figure 10, we note that the estimated resistivity on the boundary between the second and third layers became normal. The results verify the accuracy of the inversion algorithm. Thus, comparing the inversion results, we summarize the drawbacks of ignoring the IP effects in the inversion: (1) the estimated resistivity is much higher than the true values; (2) high-resistivity artifacts appear in the conductive layer (bottom left corner in Figure 7); (3) the geological shape is disturbed heavily; (4) boundary effects bring errors.

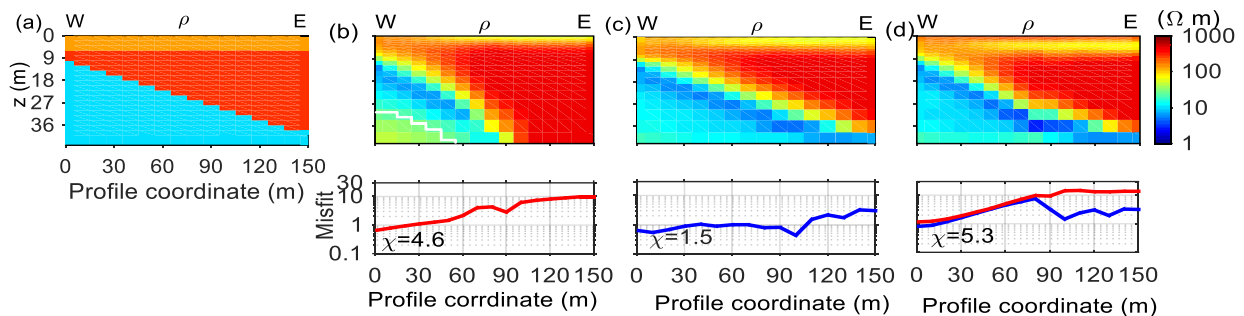


Figure 10. Comparison between the true resistivity value (a) and resistivity-inversion results of the IP responses of the moderate chargeable medium: by x -data only (b); z -data only (c); and x and z data (d). The meanings of the curves and the area are the same as in Figure 7.

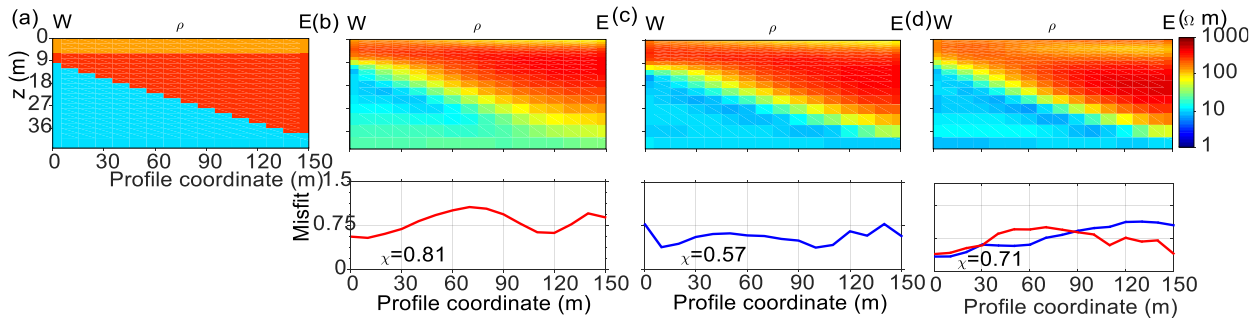


Figure 11. Comparison between the true resistivity value (a) and resistivity-inversion results of the non-IP responses of the moderate chargeable medium: x -data only (b); z -data only (c); and x and z data (d). The meanings of the curves and the area are the same as in Figure 7.

Figure 12 shows the MPA inversion results from the IP responses of the moderate chargeable medium. The resolution of the z -data and the joint inversion is superior to that of the x -data inversion. Taking the moderate IP effects into account, we can find a significant improvement in the resolution and the data are well-fitted with the z -data and joint inversion. Moreover, the main differences between the inversions are found in the first layer; with the auxiliary effects of the x -data, the resolution of ρ_{max} of the shallow layer in the joint inversion is closer to the true model.

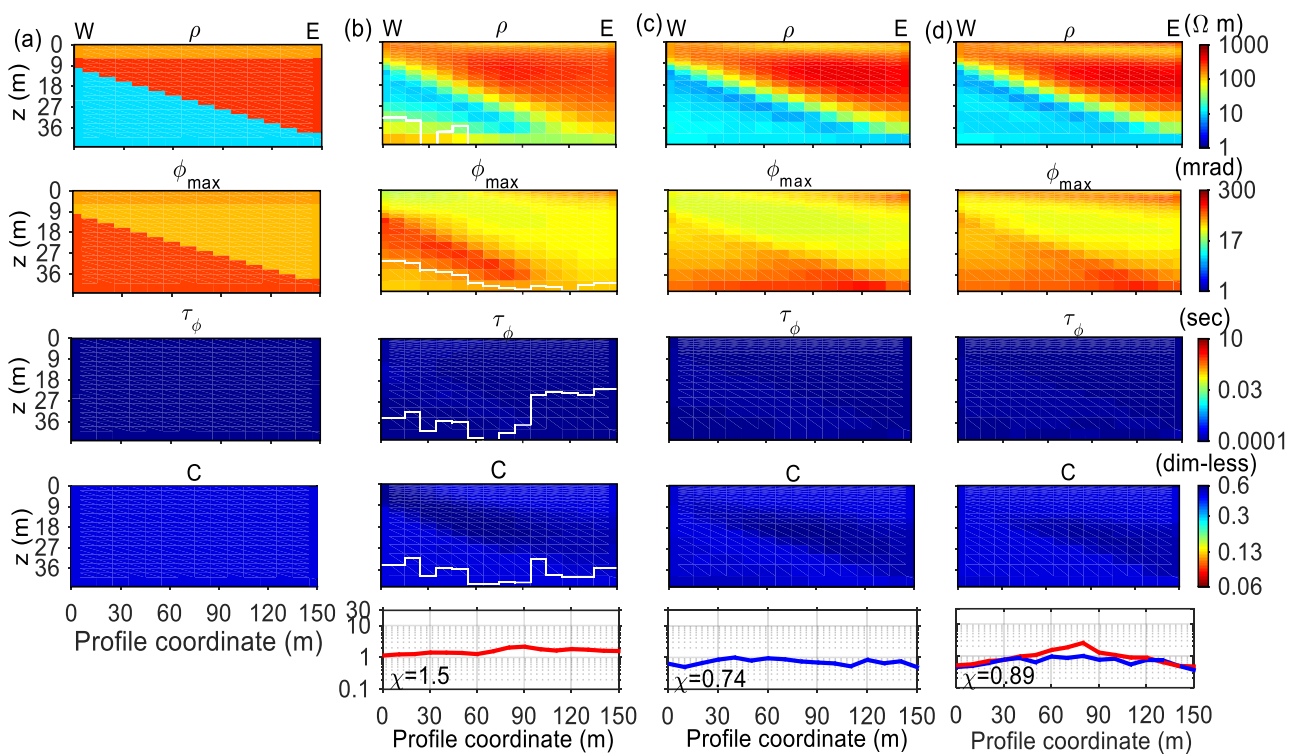


Figure 12. Comparison between the true model (a) and estimated MPA parameters of the moderate chargeable medium: by x -data only (b); z -data only (c); and x and z data (d). The meanings of the curves and the area are the same as in Figure 7.

3.2.3. Synthetic Model 3: Subtle Chargeable Medium

Figure 13 presents the resistivity-inversion results of the IP responses in the subtle chargeable medium. It seems that the results of the z -data and the joint data show that the resistivity inversion can recover the resistivity and effectively fit the data. The x -data inversion has a poor performance in the deep layer (see the DOI). We also present the results of the resistivity inversion of the non-IP responses of model 3 in Figure 14. The results also show that the z -data and joint inversion can effectively fit the non-IP responses.

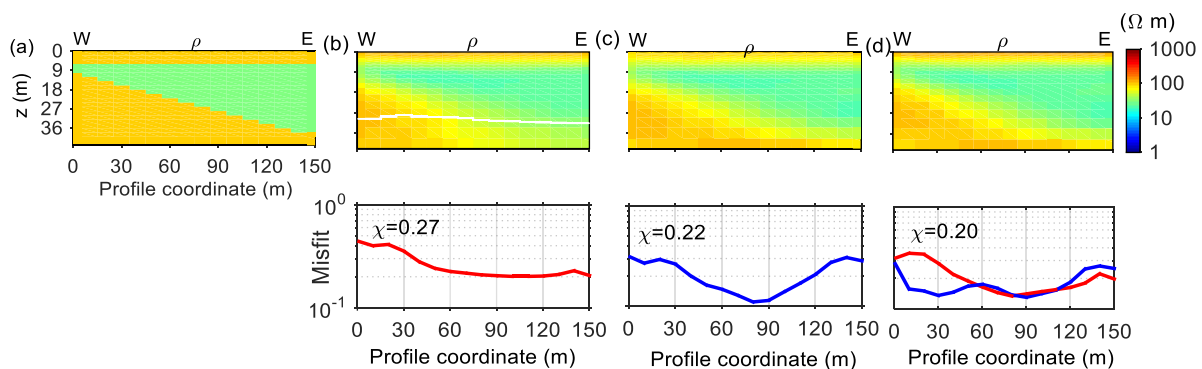


Figure 13. Comparison between the true resistivity value (a) and resistivity inversion results of the IP responses of the subtle chargeable medium: by x -data only (b); z -data only (c); and x and z data. (d) The meanings of the curves and the area are the same as in Figure 7.

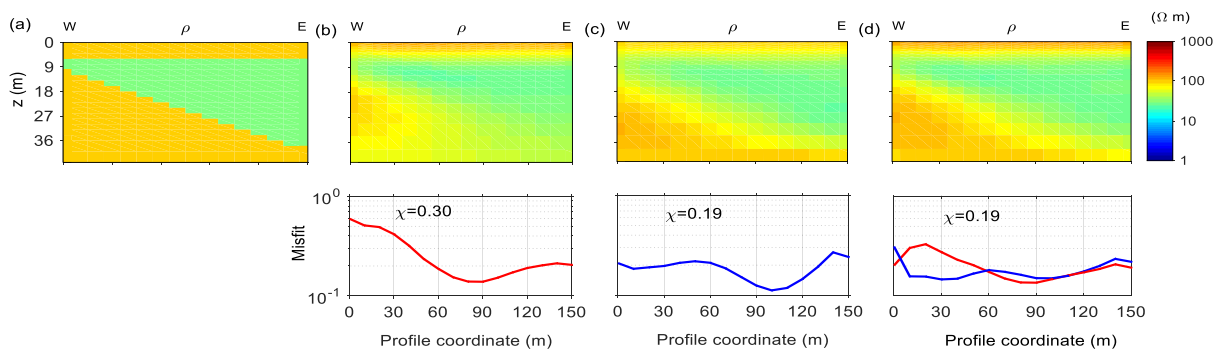


Figure 14. Comparison between the true resistivity value (a) and resistivity inversion results of the non-IP responses of the subtle chargeable medium: by x -data only (b); z -data only (c); and x and z data (d). The meanings of the curves and the area are the same as in Figure 7.

Figure 15 shows the results of MPA inversion of the IP responses. The Figure notes that the profile of ϕ_{max} in Figure 15d shows differences compared to the background ϕ_{max} . The estimated model of the most chargeable layer of the joint inversion is close to the true model, compared with the x -only and z -only inversion. The residuals of the MPA inversion are lower. For the subtle chargeable media, although resistivity inversion can achieve good fitting, we can still perform the MPA inversion by setting a lower value for chargeability, which is also effective in showing the chargeability.

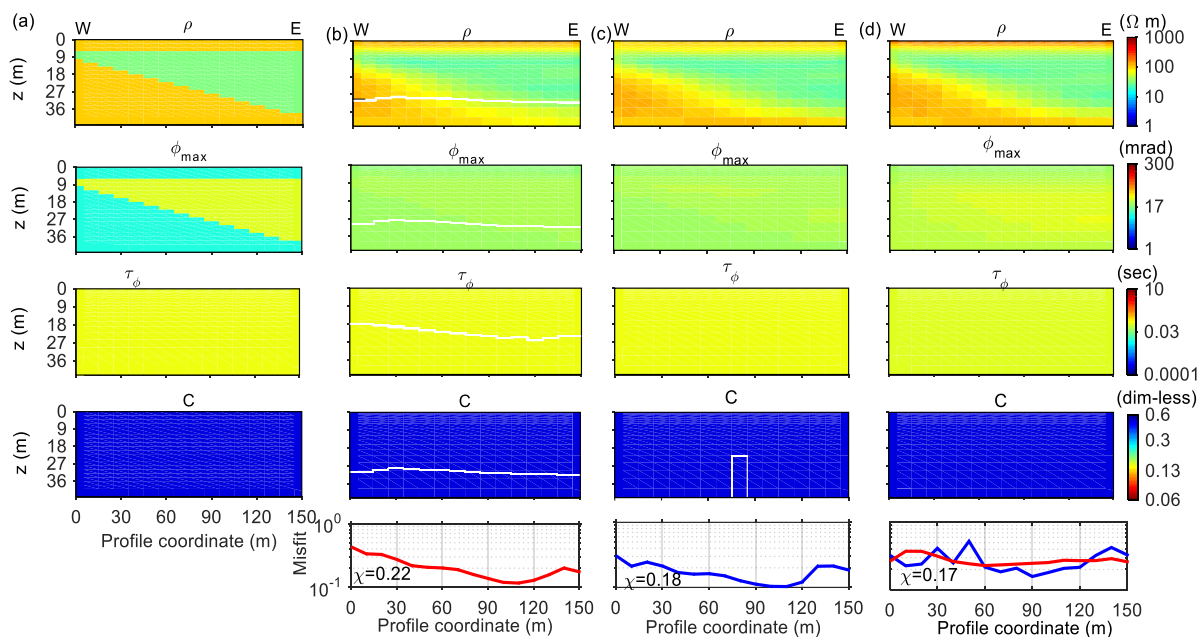


Figure 15. Comparison between the true model (a) and estimated MPA parameters of the subtle chargeable medium by x -data only (b); z -data only (c); and x and z data (d). The meanings of the curves and the area are the same as in Figure 7.

3.3. Discussion on the Recovering Capability of the Joint Inversion

From the above three synthetic models, we know that for high-polarization media, the joint inversion effectively reverted the chargeability; however, for the subtle chargeable medium (Figure 15) the estimated chargeability only showed small differences compared to the background chargeability. This finding raises another question: how does the recovering capability of the joint inversion vary for different chargeabilities? To address this issue, we set a new three-layered model. The first and third layers were rock and soil, where ρ_0 is $100 \Omega m$, ϕ_{max} is 10 mrad , τ is 100 ms , and c is 0.5 . As the second layer was more chargeable

and conductive, we set chargeability as 30, 50, 70, 100, 200, 300 mrad, respectively, while ρ_0 was 5 Ωm , τ was 100 ms, and c was 0.5. We performed forward modeling and inversion for each model and compared the resolution. The start values for each model used in the inversion process were the following: ρ_0 was 100 Ωm , ϕ_{max} was 10 mrad, τ was 100 ms, and c was 0.5.

A comparison between the true values and the estimated values for the different chargeabilities are presented in Figure 16. The estimated ϕ_{max} of Model 1' is 13 mrad, which is similar to the background value (10 mrad) due to the little polarization information contained. The estimated ϕ_{max} of model 2' begins to show changes compared to the background value, though the values (around 25 mrad) are lower than the true model. Nevertheless, this contrast reveals the subtle polarization medium. The results of Model 3' (70 mrad) and 4' (100 mrad) approach the true models' values and show significant differences. In terms of 200 and 300 mrad, the estimated values are close to the true models. From the results, we concluded that the minimum chargeability that can be recovered by the joint inversion is roughly 30 to 50 mrad.

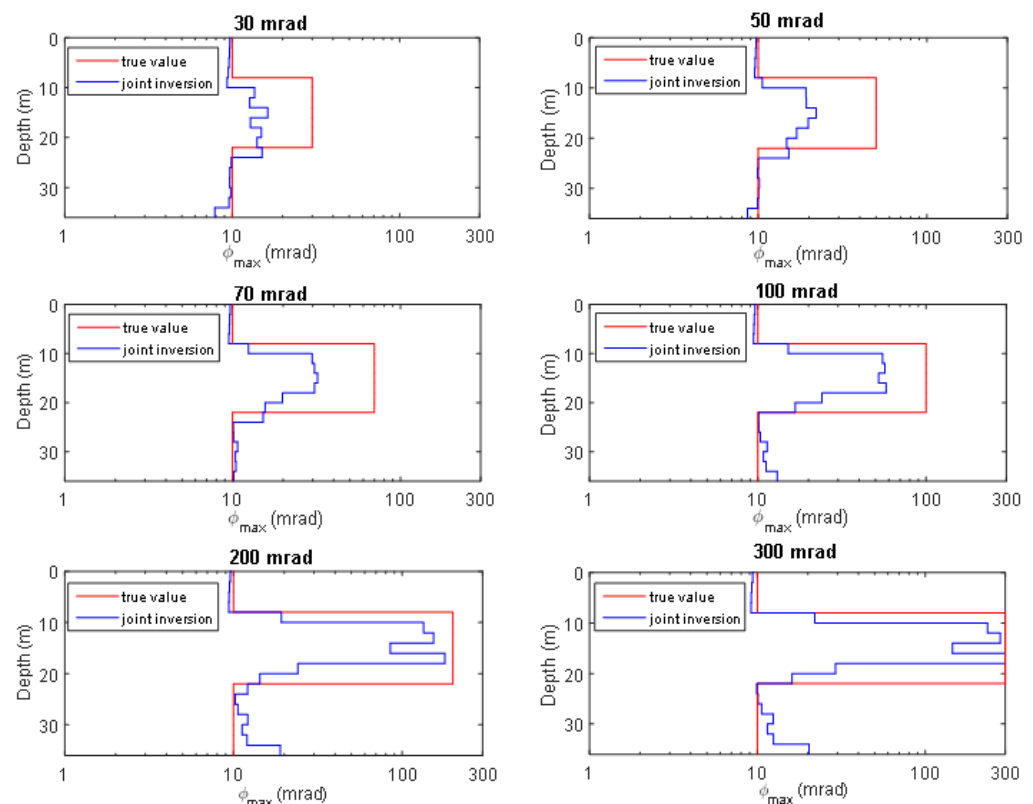


Figure 16. The recovering ability of the joint inversion for different chargeabilities: ϕ_{max} takes 30, 50, 70, 100, 200, and 300 mrad, respectively.

4. Conclusions

The effect of the horizontal component on the investigation of the subtle IP effects in the TEM data has been studied by analyzing the IP responses and inversion results. The auxiliary effects of the horizontal component contain two aspects: on the one hand, it is easier to reveal the IP features compared to the vertical component; on the other hand, introducing the horizontal component can help us to improve the resolution of the inversion.

The horizontal component reveals sign changes earlier and presents sign reversals of more than two orders of magnitude higher than the vertical component. Even when the vertical component likely does not show the IP features, the horizontal component would

decay quickly and reveal negative values. Therefore, the horizontal component contains more IP information.

For a chargeable medium, neglecting the IP effects in the inversion will result in a high-resistivity artifact and distortion at the boundary of the chargeable minerals. The vertical component inversion can easily recover the polarization parameters in deep layers, but cannot perform effectively in the shallow layers. The resolution of inversion in the shallow depth (0–30 m) is improved by adding the horizontal component. Thus, incorporating the horizontal component in measurement and interpretation can benefit the detection of the IP effects. This advantage has brought great significance to the detection of shallow chargeable media, such as frozen ground, clay ores, polluted near-surface areas, etc. These findings are also applicable in other three-component TEM systems, such as an airborne transient electromagnetic (AEM) system or a large loop TEM system with a non-central mode.

Moreover, we also analyzed the actual situation by considering different noise levels for the horizontal and vertical components in the tTEM system. The x component is much smaller than the z component, but is affected by a higher noise level. Thus, increasing the SNR of the horizontal-component signal, such as enhancing transmitter current or suppressing system noise, is of great significance for the practical application of the horizontal component.

Author Contributions: Methodology and writing—original draft preparation, Y.W. (Yanqi Wu); formal analysis, H.X.; supervision, Y.J.; validation, P.Z.; supervision, Y.W. (Yuebing Wang). All authors have read and agreed to the published version of the manuscript.

Funding: This research was funded by China Scholarship, grant number 201906170214.

Data Availability Statement: Not applicable.

Acknowledgments: The authors want to thank Esben Auken, Anders Vest Christiansen, and P.K. Maurya for their valuable suggestions, and want to thank K.E. Dalsgaard for her language polishing.

Conflicts of Interest: The authors declare no conflict of interest.

References

1. Zhdanov, M.; Alfouzan, F.; Cox, L.; Alotaibi, A.; Alyousif, M.; Sunwall, D.; Endo, M. Large-Scale 3D Modeling and Inversion of Multiphysics Airborne Geophysical Data: A Case Study from the Arabian Shield, Saudi Arabia. *Minerals* **2018**, *8*, 271. [[CrossRef](#)]
2. Chen, K.; Zhang, J.; Xue, G.; Huang, H.; Chen, W.; Hao, J.; Yue, Y. Feasibility of Monitoring Hydraulic Connections between Aquifers Using Time-lapse TEM: A Case History in Inner Mongolia, China. *J. Environ. Eng. Geophys.* **2019**, *24*, 361–372. [[CrossRef](#)]
3. Xie, W.; Yang, J.; Yao, R.; Wang, X. Spatial and Temporal Variability of Soil Salinity in the Yangtze River Estuary Using Electromagnetic Induction. *Remote Sens.* **2021**, *13*, 1875. [[CrossRef](#)]
4. Auken, E.; Pedersen, J.B.; Maurya, P.K. Environmental geophysics: A new towed geophysical transient electromagnetic system for near-surface mapping. *Preview* **2018**, *2018*, 33–35.
5. Sumi, F. The induced polarization method in ore investigation. *Geophys. Prospect.* **1961**, *9*, 459–477. [[CrossRef](#)]
6. Flis, M.F.; Newman, G.A.; Hohmann, G.W. Induced-polarization effects in time-domain electromagnetic measurements. *Geophysics* **1989**, *54*, 514–523. [[CrossRef](#)]
7. Spies, B.R. A field occurrence of sign reversals with the transient electromagnetic method. *Geophys. Prospect.* **1980**, *28*, 620–632. [[CrossRef](#)]
8. Smith, R.S.; West, G.F. Inductive interaction between polarizable conductors: An explanation of a negative coincident-loop transient electromagnetic response. *Geophysics* **1988**, *53*, 677–690. [[CrossRef](#)]
9. Macnae, J. Quantifying airborne Induced Polarization effects in helicopter time domain electromagnetics. *J. Appl. Geophys.* **2016**, *135*, 495–502. [[CrossRef](#)]
10. Smith, R.S.; West, G.F. Field examples of negative coincident-loop transient electromagnetic responses modeled with polarizable half-planes. *Geophysics* **1989**, *54*, 1491–1498. [[CrossRef](#)]
11. Zhdanov, M.S.; Endo, M.; Cox, L.; Sunwall, D. Effective-Medium Inversion of Induced Polarization Data for Mineral Exploration and Mineral Discrimination: Case Study for the Copper Deposit in Mongolia. *Minerals* **2018**, *8*, 68. [[CrossRef](#)]
12. Viezzoli, A.; Kaminski, V. Airborne IP: Examples from the Mount Milligan deposit, Canada, and the Amakinskaya kimberlite pipe, Russia. *Explor. Geophys.* **2016**, *47*, 269–278. [[CrossRef](#)]
13. Kumar, I.; Kumar, B.; Birua, S.; Dash, J.K. Inductive Induced Polarization effect in Transient Electromagnetic Surveys for Mapping Sulphide Rich Zone-A Case Study from Gurulpada Area, Singhbhum Shear Zone, Jharkhand. *J. Geophys.* **2017**, *38*, 91–100.

14. Descloitres, M.; Guérin, R.; Albouy, Y.; Tabbagh, A.; Ritz, M. Improvement in TDEM sounding interpretation in presence of induced polarization. A case study in resistive rocks of the Fogo volcano, Cape Verde Islands. *J. Appl. Geophys.* **2000**, *45*, 1–18. [[CrossRef](#)]
15. Kozhevnikov, N.O.; Antonov, E.Y. Fast-decaying IP in frozen unconsolidated rocks and potentialities for its use in permafrost-related TEM studies. *Geophys. Prospect.* **2010**, *54*, 383–397. [[CrossRef](#)]
16. Zadorozhnaya, V.; Stettler, E. Electroosmosis IP Effect as an Indicator of Compounds' Contamination: A few Case Studies. *ASEG Ext. Abstr.* **2007**, *2007*, 1–4. [[CrossRef](#)]
17. Viezzoli, A.; Manca, G.; Wjins, C. Causes and effects of the AIP trap in AEM data, *J. Appl. Geophys.* **2020**, *175*, 103970. [[CrossRef](#)]
18. Dias, C.A. Analytical model for a polarizable medium at radio and lower frequencies. *J. Geophys. Res. Atmos.* **1972**, *77*, 4945–4956. [[CrossRef](#)]
19. Debye, P.; Falkenhagen, H. Dispersion of the conductivity and dielectric constants of strong electrolytes. *Phys. Z.* **1928**, *29*, 401–426.
20. Pelton, W.H.; Ward, S.H.; Hallof, P.G.; Sill, W.R.; Nelson, P.H. Mineral discrimination and removal of inductive coupling with multi-frequency IP. *Geophysics* **1978**, *43*, 588–609. [[CrossRef](#)]
21. Zhdanov, M.S. Generalized effective medium theory of induced polarization. *Geophysics* **2008**, *73*, F197–F211. [[CrossRef](#)]
22. Marchant, D.; Haber, E.; Oldenburg, D.W. Three-dimensional modeling of IP effects in time-domain electromagnetic data. *Geophysics* **2014**, *79*, E303–E314. [[CrossRef](#)]
23. Kang, S.; Oldenburg, D.W. On recovering distributed IP information from inductive source time domain electromagnetic data. *Geophys. J. Int.* **2016**, *207*, 174–196. [[CrossRef](#)]
24. Commer, M.; Petrov, P.V.; Newman, G.A. FDTD modeling of induced polarization phenomena in transient electromagnetic. *Geophys. J. Int.* **2017**, *209*, 387–405. [[CrossRef](#)]
25. Seidel, M.; Tezkan, B. 1D Cole-Cole inversion of TEM transients influenced by induced polarization. *J. Appl. Geophys.* **2017**, *138*, 220–232. [[CrossRef](#)]
26. Ji, Y.J.; Wu, Y.Q.; Guan, S.S.; Zhao, X.J. 3D numerical modeling of induced-polarization electromagnetic response based on the finite-difference time-domain method. *Geophysics* **2018**, *83*, E385–E398. [[CrossRef](#)]
27. Nabighian, M.N. Quasi-static transient response of a conducting half-space—An approximate representation. *Geophysics* **1979**, *44*, 1700–1705. [[CrossRef](#)]
28. Steklova, K.; Lawrie, K.; Auken, E.; Christiansen, A.V.; Fiandaca, G. Overly steep decays in airborne TEM data and their link to chargeability: Example from the Howards East District, NT, Australia. *ASEG Ext. Abstr.* **2019**, *2019*, 1–5. [[CrossRef](#)]
29. Lin, C.; Fiandaca, G.; Auken, E.; Couto, M.A.; Christiansen, A.V. A discussion of 2D induced polarization effects in airborne electromagnetic and inversion with a robust 1D laterally constrained inversion scheme. *Geophysics* **2018**, *84*, E75–E88. [[CrossRef](#)]
30. Chen, T.; Hodges, G.; Smiarowski, A. Extracting subtle IP responses from airborne time domain electromagnetic data. *SEG Tech. Program Expand. Abstr.* **2015**, 2061–2066. [[CrossRef](#)]
31. Fiandaca, G.; Madsen, L.M.; Maurya, P.K. Re-parameterization of the Cole-Cole model for improved spectral inversion of induced polarization data. *Near Surf. Geophys.* **2018**, *16*, 385–399. [[CrossRef](#)]
32. Du, S.Y.; Zhang, Y.; Pei, Y.F.; Jiang, K.; Rong, L.; Yin, C.; Ji, Y.; Xie, X. Study of transient electromagnetic method measurements using a superconducting quantum interference device as B sensor receiver in polarizable survey area. *Geophysics* **2018**, *83*, 111–116. [[CrossRef](#)]
33. Ji, Y.J.; Wu, Y.Q.; Wu, Y.H.; Zhang, Y. Excitation process under the ramp-step waveform of inductive source-induced polarization method. *Geophysics* **2019**, *85*, E57–E65. [[CrossRef](#)]
34. Kirkegaard, C.; Foged, N.; Auken, E.; Christiansen, A.V.; Sørensen, K. On the value of including x-component data in 1D modeling of electromagnetic data from helicopter borne time domain systems in horizontally layered environments. *J. Appl. Geophys.* **2012**, *84*, 61–69. [[CrossRef](#)]
35. Wang, X.; Zhi, Q.; Wu, J.; Deng, X.; Huang, Y.; Yang, Q.; Wang, J. Multicomponent Transient Electromagnetic Exploration Technology and Its Application. *Minerals* **2022**, *12*, 681. [[CrossRef](#)]
36. Jang, H.; Kim, H.J.; Nam, M.J. In-loop transient electromagnetic responses with induced polarization effects of deep-sea hydrothermal deposits. *IEEE Trans. Geosci. Remote Sens.* **2016**, *54*, 7272–7278. [[CrossRef](#)]
37. Auken, E.; Foged, N.; Larsen, J.J.; Lassen, K.V.T.; Maurya, P.K.; Dath, S.M.; Eiskjær, T.T. tTEM—A towed TEM-system for detailed 3D imaging of the top 70 meters of the subsurface. *Geophysics* **2018**, *84*, E13–E22. [[CrossRef](#)]
38. Auken, E.; Christiansen, A.V.; Jacobsen, L.H.; Sørensen, K.I. A resolution study of buried valleys using laterally constrained inversion of TEM data. *J. Appl. Geophys.* **2008**, *65*, 10–20. [[CrossRef](#)]
39. Spies, B.R. Local noise prediction filtering for central induction transient electromagnetic sounding. *Geophysics* **1988**, *53*, 1068–1079. [[CrossRef](#)]
40. McCracken, K.G.; Orstaglio, M.L.; Hohmann, G.W. Minimization of noise in electromagnetic exploration systems. *Geophysics* **1986**, *51*, 819–832. [[CrossRef](#)]
41. Auken, E.; Christiansen, A.V.; Kirkegaard, C.; Fiandaca, G.; Schamper, C.; Behroozmand, A.A.; Binley, A.; Nielsen, E.; Effersø, F.; Christensen, N.B.; et al. An overview of a highly versatile forward and stable inverse algorithm for airborne, ground-based and borehole electromagnetic and electric data. *Explor. Geophys.* **2014**, *46*, 223–235. [[CrossRef](#)]

42. Ward, S.H.; Hohmann, G.W. Electromagnetic theory for geophysical applications. In *Electromagnetic Methods in Applied Geophysics*; Nabighian, M.N., Corbett, J.D., Eds.; Society of Exploration Geophysicists: Tulsa, OK, USA, 1987; Volume 1, pp. 131–312.
43. Auken, E.; Christiansen, A.V.; Jacobsen, B.H.; Foged, N.; Sorensen, K.I. Piecewise 1D Laterally Constrained Inversion of resistivity data. *Geophys. Prospect.* **2005**, *53*, 497–506. [[CrossRef](#)]
44. Kaminski, V.; Viezzoli, A. Modeling induced polarization effects in helicopter time-domain electromagnetic data: Field case studies. *Geophysics* **2017**, *82*, B49–B61. [[CrossRef](#)]
45. Fiandaca, G.; Auken, E.; Christiansen, A.V.; Gazoty, A. Time-domain-induced polarization: Full-decay forward modeling and 1D laterally constrained inversion of Cole-Cole parameters. *Geophysics* **2012**, *77*, 213–225. [[CrossRef](#)]
46. Christiansen, A.V.; Auken, E. A global measure for depth of investigation. *ASEG Ext. Abstr.* **2010**, *2010*, 1–4.

Disclaimer/Publisher’s Note: The statements, opinions and data contained in all publications are solely those of the individual author(s) and contributor(s) and not of MDPI and/or the editor(s). MDPI and/or the editor(s) disclaim responsibility for any injury to people or property resulting from any ideas, methods, instructions or products referred to in the content.